Chemical Engineering Journal 493 (2024) 152806

Contents lists available at ScienceDirect

Chemical Engineering Journal

journal homepage: www.elsevier.com/locate/cej

# Strong concentration gradient effect and weak solvation effect in thermopower enhancement in $K_3Fe(CN)_6$/ $K_4Fe(CN)_6$ aqueous electrolyte with ethanol addition

Shouze Li [a], Zhou Li [a], Dongyan Xu [b], Run Hu [a,c,*]

[a] School of Energy and Power Engineering, Huazhong University of Science and Technology, Wuhan 430074, China
[b] Department of Mechanical and Automation Engineering, The Chinese University of Hong Kong, Shatin, New Territories, Hong Kong Special Administrative Region
[c] Department of Applied Physics, Kyung Hee University, Gyeonggi-do 17104, Republic of Korea

ARTICLE INFO

*Keywords:*
Low-grade heat harvest
Thermocell
Thermogalvanic effect
Organic-water solution
Concentration gradition effect

ABSTRACT

Emerging thermocells exhibit a significant potential in low-grade heat harvesting owe to their high mV-scale thermopower, low cost, and high robustness. Fundamentally, three effects contribute to the thermopower enhancement of liquid thermocells, i.e. original concentration effect, solvation effect, and normalized concentration gradient effect. Yet, the contribution of the solvation effects and the normalized concentration gradient in organic solvents remains a subject of debate. In this paper, we integrate experiments, spectral analysis, and electrochemical theory to demonstrate that the normalized concentration gradient dominates the enhancement of thermopower in the investigated organic solvents, whereas the solvation effect is weak. Further, the introduction of ethanol results in a thermosensitive solubility of $K_4Fe(CN)_6$ and a minimal concentration at the cold end, which establishes a huge substantial normalized $Fe(CN)_6^{4-}$ concentration gradient and increases the Seebeck coefficient to 3.4 mV/K. Simultaneously, the precipitation resulting from the introduction of an organic solvent notably diminishes the heat convection within the system. As a result, the optimized TC-35EtOH system yields a *ZT* value (0.094) and Carnot-relative efficiency (2.52 %) that are 7 times greater than those of its initial counterpart. Additionally, the system's high power density of 3.64 $W/m^2$ suggests its potential for harnessing low-grade heat waste energy.

## 1. Introduction

Abundant low-grade thermal energy is ubiquitously distributed in nature [1]. Harnessing low-grade thermal energy is crucial in addressing global energy and environmental challenges [2]. In recent decades, thermoelectric generators made of semiconductor materials have been extensively studied for converting waste heat into electricity based on the Seebeck effect [3–5]. However, the application of thermoelectric generators is constrained by the relatively low Seebeck coefficient (*Se*) of ~ 100 μV/K [6–10], high cost of manufacturing, and the rarity of certain semiconductor materials [11–15].

Alternatively, the thermogalvanic cell, commonly referred to as the thermocell, is a promising solution to replace the conventional thermoelectric generators [16–18] with merits like high ~ mV/K Seebeck coefficient, cost effectiveness [19–21]. The typical thermocell consists of two electrodes and electrolyte containing a redox couple. Both the electrodes and the electrolytes are cheap and easy for scalable manufacturing [22]. As the benchmark for P-type thermocell, the 0.4 M $K_3Fe(CN)_6$/ $K_4Fe(CN)_6$ aqueous thermocell (TC) with $Se \sim 1.4$ mV/K has been studied extensively [23–36]. When a temperature gradient is applied across two electrodes, the equilibrium of reversible reactions between the redox couple is disrupted, leading to a shift in the electrode reactions in the opposite direction as shown in Fig. 1a. This shift results in the generation of an electric potential difference that can output current for constant discharging. Similar to semiconductor thermoelectric generators, the thermopower (commonly referred to as Seebeck coefficient) [35] of thermocell is defined as

$$Se = -\frac{E_H - E_C}{T_H - T_C} \quad (1)$$

with $E_H$ and $E_C$ correspond to the voltage of the hot electrode at temperature $T_H$ and the cold electrode at temperature $T_C$, respectively. To

* Corresponding author at: School of Energy and Power Engineering, Huazhong University of Science and Technology, Wuhan 430074, China.
*E-mail address:* hurun@hust.edu.cn (R. Hu).

https://doi.org/10.1016/j.cej.2024.152806
Received 2 February 2024; Received in revised form 27 May 2024; Accepted 2 June 2024
Available online 3 June 2024

generate a useful voltage of 1 to 5 V in a room temperature environment, researchers have employed various methods to enhance the *Se* of the thermocell [37,38]. The enhancement of *Se* can be expressed (Note S1) as the solvation-related entropy difference ($\Delta Sr$) and the concentration-related entropy difference ($\Delta Cr$) of the thermocell [22,39], i.e. $\Delta Se = (\Delta Cr - \Delta Sr)/nF$, where $\Delta Se$ is the thermopower difference between the studied system and corresponding aqueous electrolyte, the $n$ is the number of transferred electrons and $F$ is Faraday's constant respectively. To increase *Se* of thermocells, the strategy is to adjust $\Delta Sr$ or $\Delta Cr$, which are dominated by the solvation and the concentration of Redox ions respectively. In comparison with the control group (1.4 mV/K), Zhou group [22] utilized $Gdm^+$ cations to induce the $K_2[C(NH_2)_3]_2Fe(CN)_6{\cdot}6H_2O$ crystal of a highly thermosensitive solubility, where crystalizes at the cold end and dissolves at the hot end in order to create a concentration gradient of ions and increase the concentration-related entropy difference $\Delta Cr$ to improve *Se* to 3.78 mV/K. Additionally, Zhou group [40] also achieved a tripled *Se* (4.2 mV/K) by adding urea and GdmCl to $K_3Fe(CN)_6/K_4Fe(CN)_6$ aqueous electrolyte. In $K_3Fe(CN)_6/K_4Fe(CN)_6$ and $Fe(ClO_4)_3/Fe(ClO_4)_2$ systems, Kim [41] and Sun [42] groups investigated the *Se* enhancement of organic solvents and attributed it to ionic solvation effect. These methods are built on altering the solvation-related entropy *Sr* of ions by changing the solvent molecule configuration around the ions. However, there are still some open question in previous studies. The solvation effects observed in previous studies rely on molecular dynamics and the enhancement of *Se*. Nevertheless, these methods are made questionable by the significant influence of selective force fields and the potential concentration gradient effects. The direct observation of solvation effect is lacking and the effect of organic solvents on the solubility of electrolytes [43,44] remains unexplored yet. Moreover, the establishment of concentration gradients is centered on the unusual thermosensitive crystals as the solute ($K_2[C(NH_2)_3]_2Fe(CN)_6{\cdot}6H_2O$ [22], $(NH_4)_2Cu(SO_4)_2{\cdot}6H_2O$ [45]), while the effect of solvent remains undiscussed.

In this study, we demonstrate the *Se* enhancement through solvent design by adding varying organic solvents into $K_3Fe(CN)_6/K_4Fe(CN)_6$ aqueous electrolyte, revealing a synergic mechanism with a strong normalized concentration gradient effects to increase $\Delta Cr$ (Fig. 1a) and a weak solvation effect to decrease $\Delta Sr$ respectively. The addition of ethanol (EtOH) molecules changes the ionic solubility to induce the $K_4Fe(CN)_6$ crystallization, leading to a minimal concentration of $Fe(CN)_6^{4-}$ at the cold end and a large normalized concentration gradient ($C_{Fe(CN)_6^{4-},H}/C_{Fe(CN)_6^{4-},C}$), which results in a significant difference $\Delta Cr$ and dominates the thermopower enhancement. The direct observation of the solvation effect is demonstrated via the Raman shift of $Fe(CN)_6^{3-}$ and $Fe(CN)_6^{4-}$ ions in diverse solvent. After removing the precipitate to eliminate the concentration effect, we measure the *Se* of supernatant, revealing the competitive solvation effect and original concentration effect. The optimized TC-35EtOH showcases a high $Se = 3.4$ mV/K and remarkable power output of 3.67 W/m$^2$. Furthermore, the thermoelectric figure of merit (ZT) of TC-35EtOH is increased by 7-fold to 0.094, leading to a substantial enhancement in its overall performance. By adding 35 % EtOH, the optimized thermocell system (TC-35EtOH) showcases a high $Se = 3.4$ mV/K and remarkable power output of 3.67

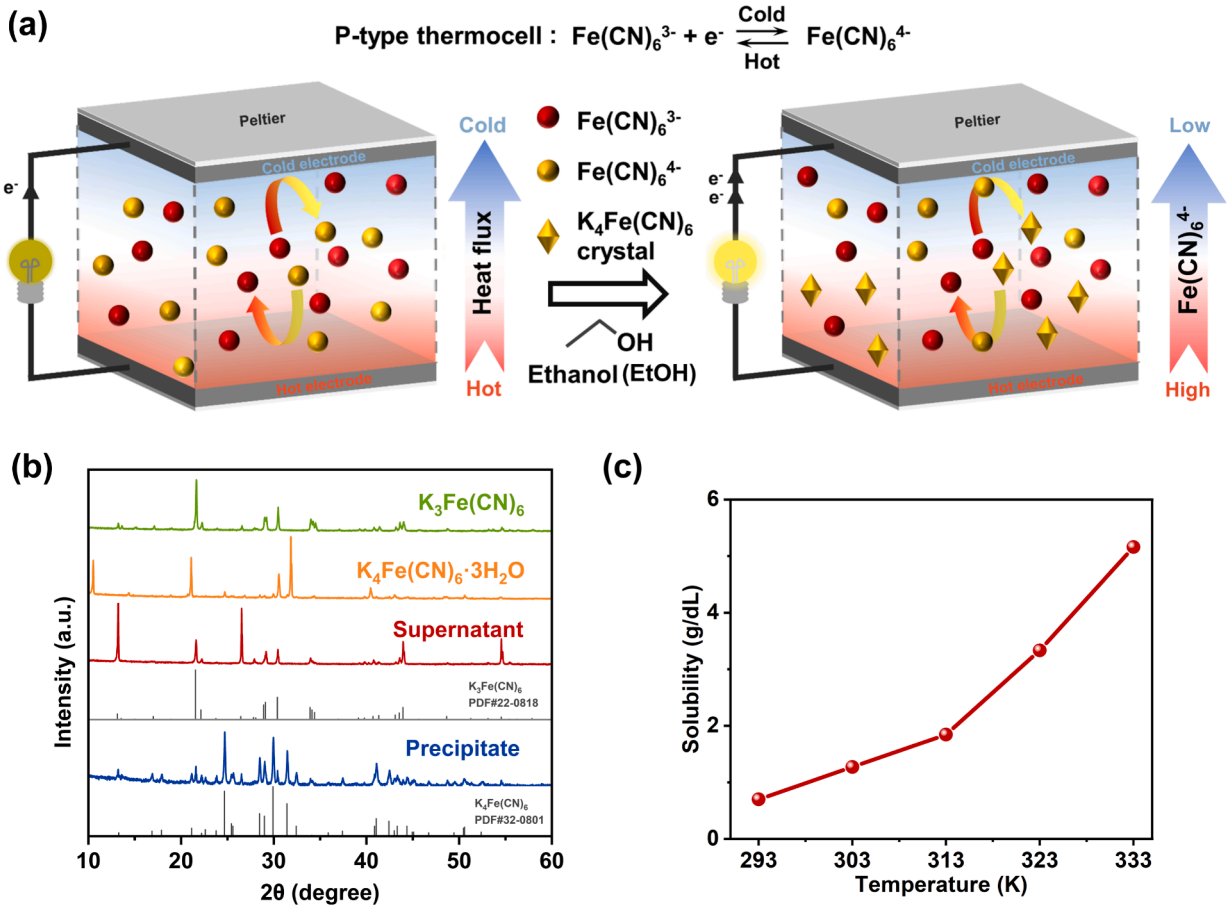


**Fig. 1.** (a) Schematic of EtOH inducing $Fe(CN)_6^{4-}$ crystallization and enhancement of the thermogalvanic effect in the 0.4 M $K_3Fe(CN)_6/K_4Fe(CN)_6$ system. (b) XRD spectra for pure $K_3Fe(CN)_6$, $K_4Fe(CN)_6{\cdot}3H_2O$ and dried powders from the supernatant and precipitate in the TC-35EtOH electrolyte. The supernatant and the precipitate corresponding reference patterns, showing their main ingredients are $K_3Fe(CN)_6$ and $K_4Fe(CN)_6$, respectively. (c) Within the operational temperature range of thermocell, the solubility of $K_4Fe(CN)_6{\cdot}3H_2O$ crystals in the mixed solvent of water and EtOH with a volume ratio of 65:35. Error bars denote SD from repeated measurements for three times at the same temperatures.

W/m$^2$, almost 2.5-fold and 2-fold enhancement compared to the original thermocell without EtOH (TC). Furthermore, the thermoelectric figure of merit (ZT) of TC-35EtOH is increased by 7-fold to 0.094. Our work offers profound and comprehensive insights into organic aqueous thermocells and paves avenues for designing solvents in thermocells, exhibiting great potential for low-grade thermal energy harvesting.

## 2. Experimental section

### 2.1. Material

All chemical reagents were purchased from Aladdin Bio-Chem Technology Co, Ltd. (China) and used without further purification. These included potassium ferrocyanide ($K_4Fe(CN)_6{\cdot}3H_2O$, potassium hexacyanoferrate(ii) trihydrate, ≥99.5 %), potassium ferricyanide ($K_3[Fe(CN)_6]$, potassium hexacyanoferrate(iii), ≥99.5 %), ethanol (EtOH, ≥99.7 %), acetone, acetonitrile (ACN), N,N-dimethylacetamide (DMA), N,N-dimethylformamide (DMF), methanol (MeOH) and ethylene glycol (EG). Graphite sheets were purchased from Graphite Material Company, Ltd. (China). The test solutions were freshly prepared for all experiments.

### 2.2. Fabrication of TC/TC-35EtOH devices

Firstly, a 0.4 M solution of $K_3Fe(CN)_6/K_4Fe(CN)_6$ electrolyte (TC) was prepared by dissolving 131.67 g of potassium ferricyanide ($K_3Fe(CN)_6$) and 168.96 g of potassium ferrocyanide trihydrate ($K_4Fe(CN)_6{\cdot}3H_2O$) in 1 L of deionized water. To optimize the electrolyte, it was further enhanced by adding 350 mL of ethanol to a mixture consisting of 650 mL of the aforementioned electrolyte solution (TC-35EtOH).

Typically, a planar single cell was used to demonstrate the thermoelectric performance of the TC/TC-35EtOH (Fig. 1a). The polymeric methyl methacrylate (PMMA) frame is filled with 0.4 M $K_3Fe(CN)_6/K_4Fe(CN)_6$ electrolyte/optimized electrolyte and both sides are sealed with 0.5 cm graphite plate to form TC/TC-35EtOH, where the cross-sectional area of the thermocell is 9 cm$^2$ and the distance between the two electrodes is 1.5 cm. The thermocouple for temperature measurement is fixed to the electrode- electrolyte interface. A temperature gradient was formed across the whole cell by placing a ceramic heating plate on the bottom and a Peltier element on the top.

### 2.3. Material characterizations

The solubility (defined as g per 100 mL mixed solvent) of the $K_4Fe(CN)_6$ crystals at different temperatures was directly measured. Typically, the crystals were gradually added to 30 mL mixed solvent at different temperatures and thermostatically incubated until the solution was saturated. In addition, the ion concentration gradients under different temperature gradients were measured by UV–Vis-NIR spectrophotometry (Shimadzu UV-3600Plus). Under a certain temperature gradient, we extracted a trace solution (10 μL) in situ near the cold electrode and the hot electrode respectively. Because the absorption strength of the extraction solution far exceeds the upper limit of the spectrometer. After the extraction solution is diluted 100 times, the absorption spectrum is measured by UV–Vis-NIR spectrophotometry to determine the ion concentration. The crystal structure of the samples was analyzed by X-ray diffraction (XRD, PANalytical B.V. X'Pert3 Powder diffractometer). The supernatant and precipitate were separated by extraction filtration, and both were dehydrated through lyophilization for 48 h. Finally, the dried powders from the supernatant and precipitate were milled before being characterized by XRD. The redox reaction mechanisms for TC and TC-35EtOH were investigated by using electrochemical workstation (Jiangsu Donghua Analytical Instrument Co., Ltd. DH7001A). Various electrolyte solutions were prepared by thoroughly blending (1-x%) volume of TC electrolyte with x% volume of an organic solvent. The supernatant obtained from filtering these electrolytes was utilized for conducting Fourier transform infrared spectroscopy (FTIR) and Raman spectroscopy analyses. FTIR (Thermo Scientific, Nicolet iS50R) was used to analyze the characteristic spectra of $Fe(CN)_6^{3-}/Fe(CN)_6^{4-}$ redox couple by the potassium bromide (KBr, Sigma Aldrich) method. Raman spectra were recorded with a LabRAM HR800 laser Raman spectrometer using a laser excitation of 532 nm.

### 2.4. Electrical measurement

A Keithley 2700 instrument was utilized to measure and record temperature, voltage, and current at a sampling rate of 1 s per point. The Seebeck coefficient of the thermocell is determined by analyzing the open circuit voltage response during the dynamic heating process. In all tests, the cold end temperature was stabilized at the origin temperature ($T_c = T_O = 298$ K) without any specific instructions, while the thermoelectric potential was measured by incrementally increasing the hot end temperature. All tests were conducted with the cold end positioned above the hot end, unless specified otherwise. To establish current–voltage curve, the thermocell with fixed temperature gradient is connected to various resistances, and precise measurements are taken for current and voltage across the resistor. Subsequently, utilizing these corresponding current and voltage values, both power-voltage curve and conductivity of thermocell can be calculated with precision. For other performance indicators, see Note S1 in SI.

### 2.5. Effective thermal conductivity measurement

Unlike solid substances, liquids possess considerable fluidity, which leads to thermal convection that affects the heat transfer of the system. Therefore, when assessing heat dissipation in thermal cells, it is imperative to directly measure the effective thermal conductivity $\lambda_{eff}$ of the liquid thermal cell rather than relying on inherent thermal conductivity values of electrolyte [22]. In this study, we used the steady-state method to accurately determine $\lambda_{eff}$ using the device shown in Fig. S7a. The cell had a cross-sectional area of 9 cm$^2$, and a distance of 1.5 cm between the two sides. The temperature profile for device was captured using an infrared camera (FLIR SC620) and the image processing software (FLIR QuickReport 1.2). To ensure that the area where the infrared camera records had the same thermal gradient as the electrolyte, we sealed the side wall with a 0.5 mm thick polycarbonate (PC) sheet. Furthermore, two identical PC boards with a thickness of 8 mm are positioned parallel at both top and bottom as heat transfer walls. An electrical heating plate on the bottom and a water-cooled plate on the top to formed a temperature gradient. Additionally, to prevent any heat input flow from escaping into the surrounding environment, the side walls of the device were covered with foam insulation that was 2 cm thick. The device was designed for heat transfer only through intermediate electrolytes. In a state of stability, according to Fourier's law:

$$\lambda_{eff}\left(\frac{\partial T}{\partial h}\right)_{electrolyte} = \lambda\left(\frac{\partial T}{\partial h}\right)_{PC} \quad (2)$$

The material thermal conductivity of PC wall is measured as $\lambda = 0.21$ W/(m·K). The effective thermal conductivity of the electrolyte can be calculated using Eq. (2) when a steady-state temperature gradient ($\partial T/\partial h$) is reached across the walls of the PC and the electrolyte.

## 3. Results and discussion

The conventional thermocells primarily consist of a redox couple of ions that possess similar physical and chemical properties, thereby making it challenging to enhance the $\Delta Sr$ between the oxidized ions and the reduced ions, as well as their coexisting concentration [38]. Utilizing the competitive effect between ions and an organic solvent such as EtOH is a simple and effective method to enhance thermopower.

Specifically, the inclusion of EtOH induces alterations in ionic

solubility, resulting in the formation of a TC-EtOH system that comprises a supernatant phase and a precipitated phase (Fig. S1). XRD analysis (Fig. 1b) confirms that the main components of the supernatant phase and the precipitate phase are $K_3Fe(CN)_6$ and $K_4Fe(CN)_6$, respectively. The addition of EtOH was shown to decrease the solubility of $K_4Fe(CN)_6$. The solubility of $K_4Fe(CN)_6$ in the mixed solvent exhibits a temperature-dependent and positive correlation within the operational temperature range of thermocell (Fig. 1c). Therefore, a stable $Fe(CN)_6^{4-}$ ion concentration gradient can be attained in a thermocell through astute design. In a TC-EtOH system where the top electrode is cold and the bottom electrode is hot, $Fe(CN)_6^{4-}$ spontaneously precipitates and undergoes crystallization on the cold side (top), leading to a reduced local $Fe(CN)_6^{4-}$ concentration near the cold electrode, which enhances the reduction reaction of $Fe(CN)_6^{3-} + e^- \rightarrow Fe(CN)_6^{4-}$. Due to the force of gravity, the $K_4Fe(CN)_6$ crystals move from cold side (top) to hot side (bottom). Subsequently, $K_4Fe(CN)_6$ crystals redissolves on the hot side (bottom), resulting in a high local $Fe(CN)_6^{4-}$ concentration near the hot electrode that enhances the oxidation reaction of $Fe(CN)_6^{4-} \rightarrow Fe(CN)_6^{3-} + e^-$.

Various characterization methods were employed to validate the aforementioned conjecture. According to cyclic voltammetry (Fig. S2), the presence of precipitates leads to an increase in both the potential and current of the redox reaction, indicating an elevated concentration of the reducing substance [46–48]. The concentration profiles of $Fe(CN)_6^{4-}$ and $Fe(CN)_6^{3-}$ at various temperature differences were revealed by UV–Vis spectroscopy as shown in Fig. 2a. As the temperature rises, the absorbance at approximately the 218 nm ($Fe(CN)_6^{4-}$) wavelength gradually increases. The results confirmed a stable $Fe(CN)_6^{4-}$ ion concentration gradient exists from the hot end to the cold end in the TC-35EtOH system in working condition. At the same time, the $Fe(CN)_6^{3-}$ ion concentration (420 nm) at the hot and cold ends is nearly equal. Unfortunately, it is difficult to directly calculate the concentration of $Fe(CN)_6^{4-}$ using Beer-Lambert's law due to the absorption of EtOH at 218 nm and the effect of large $Fe(CN)_6^{3-}$ concentration ($C_{Fe(CN)_6^{3-}} > 0.01\ M > C_{Fe(CN)_6^{4-}}$).

The thermoelectric performance of the thermocell was measured using a typical cuboid cell as shown in Fig. 1a. The Seebeck coefficient *Se* of the thermocell is determined by analyzing the open circuit voltage response during the dynamic heating process (Fig. S3). During the steady-state, the crystals precipitated to the bottom of the cell, while the electrolyte settled at the top (Fig. 1a). Owing to the $Fe(CN)_6^{4-}$ concentration gradient and the increase of $\Delta Cr$, the *Se* for the TC-EtOH is much higher than that for the pristine TC (Fig. 2b). Throughout the experimental range of volume concentrations (10 % to 40 %), the Seebeck effect of TC-φEtOH was observed to be stronger than that of TC. The optimized amount of EtOH addition was investigated to achieve the highest *Se*, which was found to be at approximately 35 % volume concentration. Upon the introduction of EtOH, a higher amount of $K_4Fe(CN)_6$ precipitated, leading to a decrease in $Fe(CN)_6^{4-}$ concentration at the cold end (Fig. S1). This change results in an increase in both the concentration-related entropy difference (ΔCr is positively related to $C_{Fe(CN)_6^{4-},H}/C_{Fe(CN)_6^{4-},C}$) and *Se*, reaching a peak at approximately 35 % volume concentration of EtOH. Beyond this point, excess EtOH causes the precipitation of $K_3Fe(CN)_6$ (Fig. S1) and a gradient in $Fe(CN)_6^{3-}$ concentration, leading to a decrease in $\Delta Cr$ and *Se*. The maximum Seebeck coefficient value for the TC-35EtOH system is approximately 2.5 times higher than that of the TC system (3.4 mV/K vs. 1.4 mV/K) (Fig. 2c).

In practical applications, the focus is often on the output power of the system [49]. The current–voltage curve and corresponding power output of TC and TC-35EtOH (Fig. 2d) can be measured by connecting different resistors at both ends of the thermocell. At $\Delta T = 40$ K, the maximum power density ($P_{max}$) for the TC-35EtOH is 3.64 W/m$^2$,

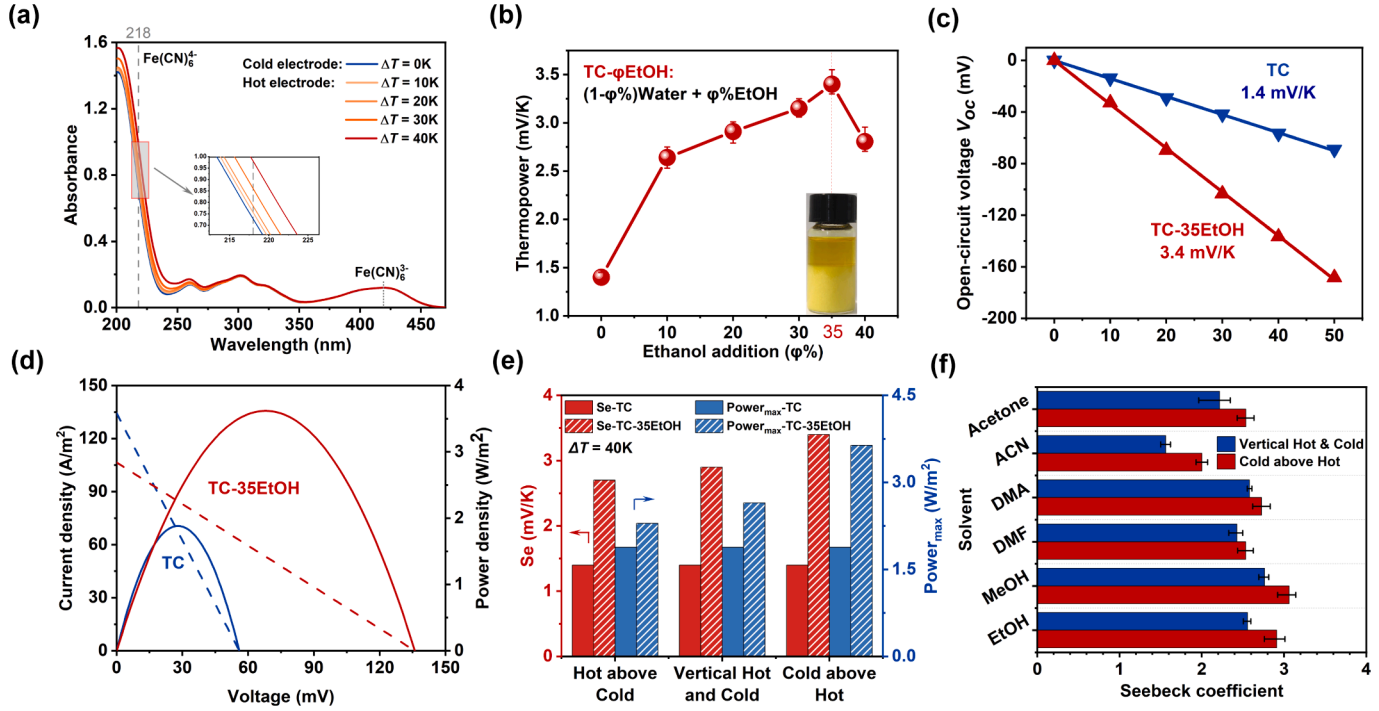


**Fig. 2.** (a) UV–Vis spectra of solution at cold and hot electrode in TC-35EtOH under different temperature difference. The extracted solution samples were diluted 100 times by water for UV–Vis analysis. The characteristic absorption peaks of $Fe(CN)_6^{4-}$ and $Fe(CN)_6^{3-}$ are located at ~ 218 nm and 420 nm, respectively. (b) The thermopower with the addition of EtOH at φ% volume concentrations in the 0.4 M $K_3Fe(CN)_6/K_4Fe(CN)_6$ electrolyte. Error bars denote SD from repeated measurements for five times at the same temperatures and EtOH volume concentrations. (c) Open-circuit voltage ($V_{oc}$) of the TC and TC-35EtOH at different values of temperature difference $\Delta T$ ($T_C = 298$ K). (d) Current-voltage curve (Dotted line) and corresponding power output (Solid line) of TC (blue) and TC-35EtOH (red) at $\Delta T = 40$ K. (e) The *Se* and maximum power output density $P_{max}$ of TC and TC-35EtOH at different orientations and $\Delta T = 40$ K. (f) The *Se* of the 0.4 M $K_3Fe(CN)_6/K_4Fe(CN)_6$ electrolyte in various mixed solvents was measured at different orientations. The mixed solvent comprises 80 % water and 20 % specific solvent by volume. Error bars denote SD from repeated measurements for three times at the same solvent.

approaching twice the $P_{max} = 1.88$ W/m$^2$ of the pristine TC.

Additionally, the performance of TC-35EtOH is dependent on its orientation. We assessed the thermoelectric properties of the TC-35EtOH with three unique orientations as shown in Fig. 2e. The thermoelectric device outperforms when the cold electrode is positioned above the hot electrode. This superiority is attributed not only to heat convection [50], but also to gravity's role in inducing crystallization movements, resulting in a larger $\Delta Cr$ in this configuration. This strategy demonstrated consistent success across various solvents tested in experiments (Fig. 2f), establishing the universal applicability of building a stable normalized concentration gradient through organic solvents.

It is worth noting that the thermoelectric properties of TC-35EtOH with different orientations are superior to those of TC (Fig. 2e). What dominates the thermopower enhancement of TC-35EtOH? It is necessary to further confirm the contribution of various components including special property of precipitation, effect of original concentration, solvation effects [33,41], and normalized concentration gradients in TC-35EtOH.

First, we examined whether the improvement of the thermopower in TC-35EtOH was dominated by the precipitation or the solvent, by controlling variables. The results depicted in Fig. 3a indicate that the thermopower remains nearly identical with the addition of precipitation and $K_4Fe(CN)_6$ crystals. The effect of precipitation mirrors that of crystals, implying that the precipitation in TC-35EtOH is not distinctive, consistent with the conclusion above (Fig. 1b). On the other hand, the thermopower exhibited a substantial boost in the supernatant of TC-35EtOH (~3.4 mV/K) compared to the TC solvent (~1.8 mV/K). Hence, it is evident that the unique properties of solvents in TC-35EtOH dominates the enhancement in the thermopower.

For reaction $Fe(CN)_6^{4-} \rightleftharpoons Fe(CN)_6^{3-} + e^-$, the thermopower enhancement in TC-φEtOH can be expressed as (Note S1):

$$\Delta Se = \frac{R\ln\left(\frac{C_{Fe(CN)_6^{4-},O}}{C_{Fe(CN)_6^{3-},O}}\right) - \Delta Sr + \frac{T_H}{T_H - T_C} R\ln\left(1 + \Delta C \Big/ C_{Fe(CN)_6^{4-},O}\right)}{nF} \quad (3)$$

where the subscripts "O" indicate the original concentration (bulk concentration) and $\Delta C$ is the concentration difference between hot and cold ends caused by temperature difference.

The influences induced by the solvent encompass include the original concentration ($C_O$) effect, the solvation effect ($\Delta Sr$) and the normalized ion concentration gradient effect ($1 + \Delta C/C_{Fe(CN)_6^{4-},O}$) arising from temperature differences. To observe the atomic vibration and the solvation effect directly [51], we measured Raman spectroscopy of ions in various solvents. The Raman shifts of ions $Fe(CN)_6^{4-}$ and $Fe(CN)_6^{3-}$ in various organic-aqueous solvents differ from those of the same ions in pure water (Fig. 3b, d). The results indicate the presence of a solvation effect in organic-aqueous solutions.

However, further investigation is required to determine its contribution to the thermopower. Out of the three effects, only the ion concentration gradient effect is dependent on the excess solid solute, since the normalized concentration gradient effect depends on the dissolution of the solid solute at the hot end [51], when we fixed the cold end temperature and raised the hot end temperature ($T_H > T_c = T_O = 298$ K). In addition, the solvation effect can be eliminated by replacing the mixed solvent with water. So the supernatant was obtained by filtering

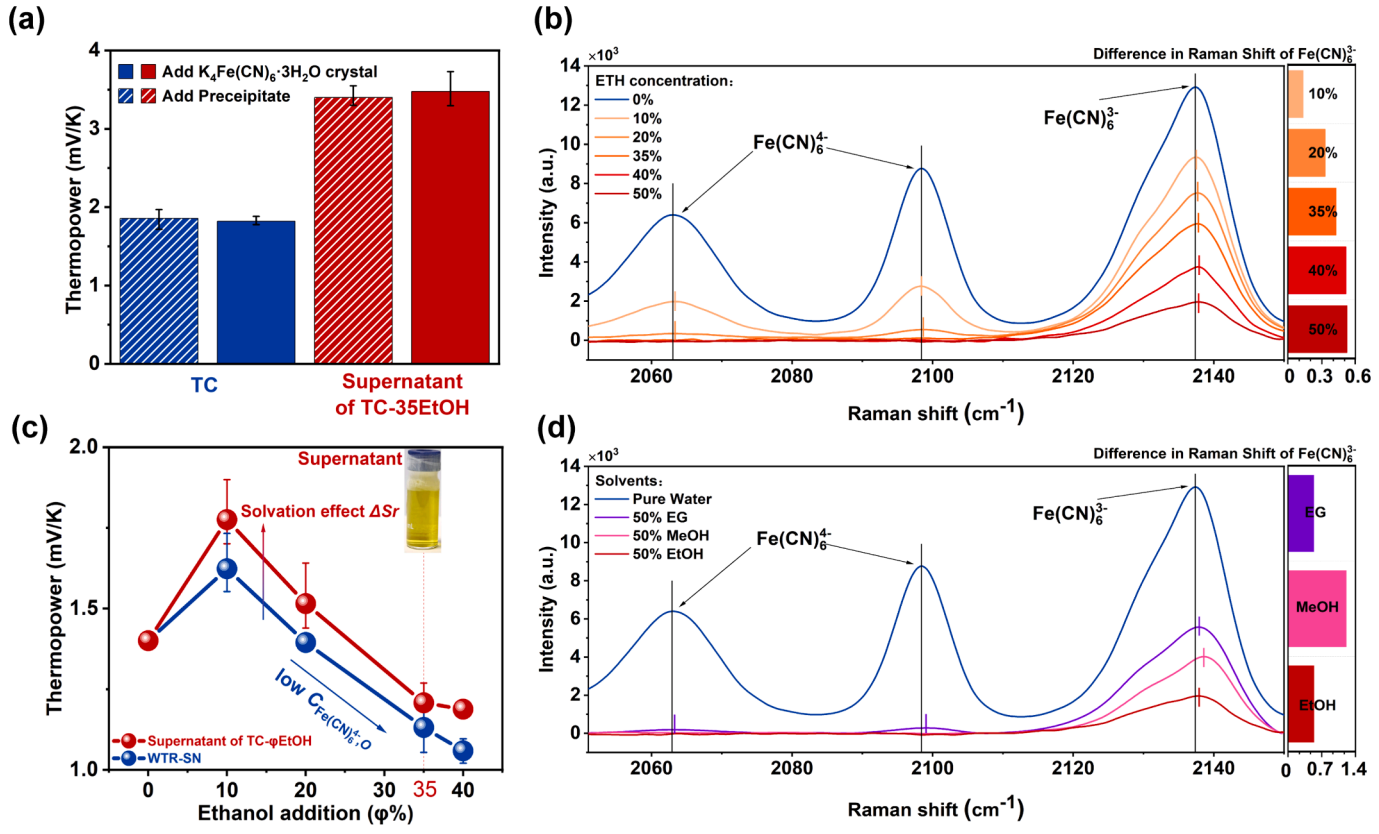


**Fig. 3.** (a) The thermopower of TC and supernatant solvents when different crystals are added. Both solids were added in equal masses and were not depleted during the test. Error bars denote SD from repeated measurements for five times under uniform conditions. (b) Raman spectra of EtOH solvents at varying volume fractions. Peaks at 2063 cm$^{-1}$ and 2098 cm$^{-1}$ corresponded to the characteristic peak of $Fe(CN)_6^{4-}$. And peaks at 2137 cm$^{-1}$ corresponded to the characteristic peak of $Fe(CN)_6^{3-}$. The peak is marked with a vertical line. The variations in Raman shifts of $Fe(CN)_6^{3-}$ among different solvents and pure water are illustrated on the right. (c) The thermopower of the supernatant in TC-φEtOH (red). The thermopower of the solution (blue), which was obtained by freeze-drying the supernatant and dissolving it using the same volume of water (WTR-SN). Error bars denote SD from repeated measurements for five times under uniform conditions. (d) Raman spectra of varying organic solvents with 50 % volume fractions.

the TC-φEtOH to remove the concentration gradient effect. Further, the solvation effect is eliminated by dissolving the solute obtained by freezing and drying the supernatant in an equal volume of water (WTR-SN). The thermopower enhancement of each system according to Eq. (3) can be expressed as

$$\begin{cases} \Delta Se_{TC-\varphi EtOH} = \dfrac{R\ln\left(\dfrac{C_{Fe(CN)_6^{4-},O}}{C_{Fe(CN)_6^{3-},O}}\right) - \Delta Sr + \dfrac{T_H}{T_H - T_C} R\ln\left(1 + \Delta C \Big/ C_{Fe(CN)_6^{4-},O}\right)}{nF} \\ \Delta Se_{supernatant} = \dfrac{R\ln\left(\dfrac{C_{Fe(CN)_6^{4-},O}}{C_{Fe(CN)_6^{3-},O}}\right) - \Delta Sr}{nF} \\ \Delta Se_{WTR-SN} = \dfrac{R\ln\left(\dfrac{C_{Fe(CN)_6^{4-},O}}{C_{Fe(CN)_6^{3-},O}}\right)}{nF} \end{cases} \quad (4)$$

The impacts of these three effects were quantified by measuring the thermopower of each system. From 0 % to 10 % EtOH, the rise in the thermopower is attributed to the change in the activity coefficient resulting from the decrease in ionic concentration, which has been observed in other studies [30,31]. As the volume fraction of EtOH increases (10 %-40 %), the thermopower of WTR-SN decreases (Fig. 3c blue line), which is attributed to the low concentration of $Fe(CN)_6^{4-}$ (Fig. 3b, S4) [30] and the reduction of the original concentration ratio $C_{Fe(CN)_6^{4-},O}/C_{Fe(CN)_6^{3-},O}$. When the volume fraction of EtOH was 35 %, the original concentration effect weakened the thermopower (1.13 mV/K vs. 1.4 mV/K).

By comparing the thermopower of the supernatant (Fig. 3c red line) as well as its corresponding WTR-SN electrolyte (Fig. 3c blue line), we estimated the effect of the solvation. In the EtOH volume fraction range from 10 % to 40 %, the thermopower of the supernatant (Fig. 3c red line) exceeds that of the corresponding WTR-SN, suggesting that the EtOH-induced solvation effect boosts the system's thermopower. In the thermopower enhancement of TC-35EtOH, the contribution of its solvation effect is approximately 1.21–1.13 = 0.08 mV/K.

However, it is worth noting that neither the solvation effect nor the original concentration effect is the key to determining the thermopower enhancement of TC-φEtOH, as the thermopower of TC-φEtOH (Fig. 2b) is significantly surpasses that of the supernatant and the WTR-SN (Fig. 3c). According to Eq. (4), the normalized concentration gradient effect dominates the thermopower enhancement of TC-φEtOH. By comparing the thermopower of TC-φEtOH (Fig. 2b) as well as its corresponding supernatant (Fig. 3c), we estimated the effect of the normalized concentration gradient. In the thermopower enhancement of TC-35EtOH, the contribution of its normalized concentration gradient effect was approximately 3.4–1.21 = 2.19 mV/K.

Further, we compare the temperature-dependent solubility of $K_4Fe(CN)_6$ in systems TC and TC-35EtOH (Fig. 4a). Although the $Fe(CN)_6^{4-}$ concentration in TC varies more with changes in temperature than that in TC-35EtOH, the normalized concentration of TC is lower since it is influenced by the significantly higher concentration ($C_{O,TC} \gg C_{O,TC\text{-}35EtOH}$) at the cold end (Fig. 4a). For its original concentration, a more accurate description is the saturation concentration of the system at the cold end. Therefore, attaining higher the concentration-related entropy difference $\Delta Cr$ necessitates not only an increased thermosensitivity of concentration but also a reduced saturation concentration at the cold end.

We validate the aforementioned conclusions in various organic aqueous solutions. The findings demonstrate that the normalized concentration gradient predominantly impacts the enhancement of the Seebeck coefficient in the majority of mixed solvents (Fig. 4b). Furthermore, we observed that the ACN mixture resulted in the lowest

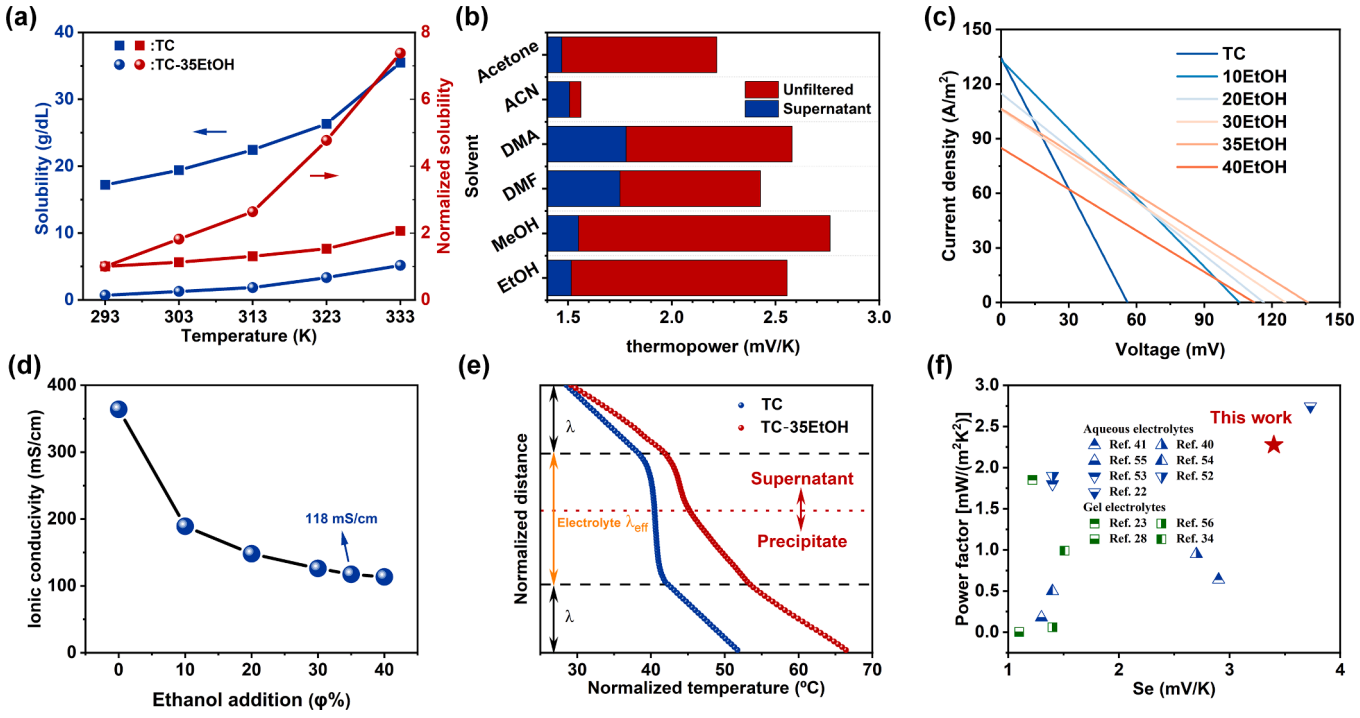


**Fig. 4.** (a) Within the operational temperature range of thermocell, the solubility and normalized solubility of $K_4Fe(CN)_6{\cdot}3H_2O$ crystals in TC and TC-35EtOH, respectively. (b) The Se of the 0.4 M $K_3Fe(CN)_6/K_4Fe(CN)_6$ electrolyte in various mixed solvents and their corresponding supernatant. The mixed solvent comprises 80 % water and 20 % specific solvent by volume. (c) Current–voltage curves for the TC and TC-φEtOH with various volume concentrations φ and their corresponding output power are shown in Fig. S6. (d) Effective electrical conductivity (σ) was calculated from the slopes of the current–voltage curves. (e) Temperature profiles of the TC and TC-35EtOH electrolyte, obtained from their corresponding infrared images (Fig. S7). (The red dot line is the interface between precipitation and supernatant.) (f) Comparison of Se and Power factor values for various thermocell systems [22,23,28,34,40,41,52–56] with aqueous or gel electrolytes (Table S1).

precipitation among all the tested solvents (Fig. S5). So we attribute the uniqueness of ACN-water solvent to increased polarity of ACN with a lesser impact on ionic solubility.

In addition to thermopower and power density, the equivalent conductivity σ and thermal conductivity $\lambda_{eff}$ of the system are also crucial, which directly affect the energy dissipation and the overall efficiency of the system [57,58]. The current–voltage curve (Fig. 4c) enables the estimation of effective electrical conductivity for thermocell systems. The effective ionic conductivity of the system decreases with the increase of EtOH as shown in Fig. 4d. The effective ionic conductivity of TC-35EtOH is 118mS/cm, which is one-third that of TC. The resistance of thermocell involves three components: the electron transport resistance at the electrode, the charge transfer resistance at the electrode and the electrolyte interface, and the ion diffusion resistance at the electrolyte [39,59]. The charge transport resistance can be reduced to a negligible level when a highly conductive material such as graphite and copper is used as an electrode. While the charge transfer resistance at the electrode and the electrolyte interface is linked to the electrode's catalytic ability and specific surface area, this is not the primary reason for the effective electrical conductivity drop. The system resistance is mainly due to the ion diffusion resistance in the electrolyte, which depends on the oxidation and reducing substances' solubility and concentration, as per the Nernst-Einstein relationship show $\sigma = \frac{Nz^2e^2}{K_BT}D$ where $N$ is the number of ions per unit volume, $z$ is the ion valence number, $e$ is the electron charge, $K_B$ is Boltzmann constant, $T$ is the temperature and $D$ is the diffusion coefficient of ions. EtOH addition leads to a decrease of ionic solubility and the bulk number of $Fe(CN)_6^{4-}$ ions (Fig. 4a, S4) which determine the conductivity.

We measured the effective thermal conductivity of the electrolyte of TC and TC-35EtOH by steady-state method [22] using the device shown in Fig. S7a. The infrared thermal image of the TC and TC-35EtOH electrolyte captured are shown in Fig. S7b–c. According to the measured temperature gradient (Fig. 4e) and Eq. (2), the effective thermal conductivity of TC and TC-35EtOH electrolytes can be calculated as 1.65 W/(m·K) and 0.46 W/(m·K), respectively. The TC liquid electrolyte undergoes intense thermal convection due to the applied temperature gradient, thereby enhancing its heat transfer [32,60]. The presence of a precipitation layer in TC-35EtOH inhibits thermal convection within the liquid electrolyte, resulting in a significantly lower effective thermal conductivity compared to that of TC. The precipitation layer in TC-35EtOH has a lower effective thermal conductivity [0.35 W/(m·K)] than that of the supernatant [0.77 W/(m·K)], which further supports the previously stated conclusion. Compared to TC, the smaller equivalent thermal conductivity allows TC-35EtOH to achieve a larger temperature difference $\Delta T$ on both sides of the electrode with the same input power $P_{in}$, which is particularly significant for practical applications.

Some comprehensive indexes are used to evaluate the overall performance of thermocell devices (Table S2). According to the Eqs. (S14-15), the figure of merit $ZT$ and the Carnot-relative efficiency $\eta_r$ of TC-35EtOH can be calculated as 0.094 and 2.52 % respectively, which is more than 7 times that of the TC system ($ZT = 0.013$ and $\eta_r = 0.34$ %). In addition, the power factor for the TC-35EtOH substantially surpasses that for major optimized thermocell systems (Fig. 4f) in the literature [22,23,28,34,40,41,52–56].

## 4. Conclusions

In summary, a large increase in Seebeck coefficient from 1.4 mV/K to 3.4 mV/K was achieved by adding ethanol solvent to a typical P-type 0.4 M $K_3Fe(CN)_6/K_4Fe(CN)_6$ REDOX system. The enhancement of the thermopower arises from the combination of the original concentration effect, solvation effect and normalized concentration effect. The results of Raman spectra directly reveal that ions $Fe(CN)_6^{3-}$/ $Fe(CN)_6^{4-}$ have different solvation structures in pure water solution and mixed solution. By integrating electrochemical theory with experiment, it is revealed that the original concentration effect and solvation effect exhibit a minor influence in TC-35EtOH. The introduction of EtOH results in a minimal solubility of $K_4Fe(CN)_6$ at the cold end and establishes a substantial normalized $Fe(CN)_6^{4-}$ concentration gradient, which in turn increases concentration-related entropy difference ($\Delta Cr$) and dominates the enhancement of thermoelectric properties in TC-35EtOH. This strategy for solvent design demonstrated consistent success across various solvents tested in additional experiments. Simultaneously, the precipitation layer hinders heat convection in the electrolyte, causing the thermal conductivity to decrease to 0.46 W/(m·K), down from the original 1.65 W/(m·K). The high Seebeck coefficient and low thermal conductivity give TC-35EtOH the figure of merit $ZT$ and the Carnot-relative efficiency of 0.094 and 2.52 %, more than seven times that of the original TC system ($ZT = 0.013$ and $\eta_r = 0.34$ %). This study examines in detail the impact of organic solvent on thermogalvanic cells and enriches insights into novel methods to improve thermoelectric properties through solvent design. The electrolytes optimized in this research exhibit excellent thermoelectric properties and hold promise for harvesting low-grade waste heats. Simultaneously, the research in this paper offers profound and comprehensive insights into organic aqueous thermocells and introduces a novel idea for designing solvents in thermocells.

## CRediT authorship contribution statement

**Shouze Li:** Writing – original draft, Investigation, Conceptualization. **Zhou Li:** Writing – review & editing. **Dongyan Xu:** Writing – review & editing. **Run Hu:** Writing – review & editing, Supervision, Conceptualization.

## Declaration of competing interest

The authors declare that they have no known competing financial interests or personal relationships that could have appeared to influence the work reported in this paper.

## Data availability

Data will be made available on request.

## Acknowledgements

The work is supported by National Natural Science Foundation of China (NSFC No. 52161160332). D.X. acknowledges the NSFC/RGC Joint Research Scheme (Project No. N_CUHK419/21) sponsored by the Research Grants Council of the Hong Kong Special Administrative Region, China.

## Appendix A. Supplementary data

Supplementary data to this article can be found online at https://doi.org/10.1016/j.cej.2024.152806.

## References

[1] S. Wei, J. Ma, D. Wu, B. Chen, C. Du, L. Liang, Y. Huang, Z. Li, F. Rao, G. Chen, Z. Liu, Constructing flexible film electrode with porous layered structure by MXene/SWCNTs/PANI ternary composite for efficient low-grade thermal energy harvest, Adv. Funct. Mater. 33 (2023) 2209806, https://doi.org/10.1002/adfm.202209806.

[2] Y. Ammar, S. Joyce, R. Norman, Y. Wang, A.P. Roskilly, Low grade thermal energy sources and uses from the process industry in the UK, Appl. Energy 89 (2012) 3–20, https://doi.org/10.1016/j.apenergy.2011.06.003.

[3] B.I. Ismail, W.H. Ahmed, Thermoelectric power generation using waste-heat energy as an alternative green technology, recent pat, Electr. Electron. Eng. Former. Recent Pat. Electr. Eng. 2 (2009) 27–39, https://doi.org/10.2174/1874476110902010027.

[4] H. Jouhara, A. Żabnieńska-Góra, N. Khordehgah, Q. Doraghi, L. Ahmad, L. Norman, B. Axcell, L. Wrobel, S. Dai, Thermoelectric generator (TEG)

technologies and applications, Int. J. Thermofluids 9 (2021) 100063, https://doi.org/10.1016/j.ijft.2021.100063.
[5] A.G. Olabi, M. Al-Murisi, H.M. Maghrabie, B.A. Yousef, E.T. Sayed, A.H. Alami, M. A. Abdelkareem, Potential applications of thermoelectric generators (TEGs) in various waste heat recovery systems, Int. J. Thermofluids 16 (2022) 100249, https://doi.org/10.1016/j.ijft.2022.100249.
[6] M. Hamid Elsheikh, D.A. Shnawah, M.F.M. Sabri, S.B.M. Said, M. Haji Hassan, M. B. Ali Bashir, M. Mohamad, A review on thermoelectric renewable energy: Principle parameters that affect their performance, Renew. Sustain. Energy Rev. 30 (2014) 337–355, https://doi.org/10.1016/j.rser.2013.10.027.
[7] L. Tzounis, M. Liebscher, R. Fuge, A. Leonhardt, V. Mechtcherine, P- and n-type thermoelectric cement composites with CVD grown p- and n-doped carbon nanotubes: Demonstration of a structural thermoelectric generator, Energy Build. 191 (2019) 151–163, https://doi.org/10.1016/j.enbuild.2019.03.027.
[8] Z. Dong, H. Liu, X. Yang, J. Fan, H. Bi, C. Wang, Y. Zhang, C. Luo, X. Chen, X. Wu, Facile fabrication of paper-based flexible thermoelectric generator, Npj Flex. Electron. 5 (2021) 1–6, https://doi.org/10.1038/s41528-021-00103-1.
[9] E. Jin Bae, Y. Hun Kang, K.-S. Jang, S. Yun Cho, Enhancement of Thermoelectric Properties of PEDOT:PSS and Tellurium-PEDOT:PSS Hybrid Composites by Simple Chemical Treatment, Sci. Rep. 6 (2016) 18805, https://doi.org/10.1038/srep18805.
[10] S. Lin, L. Zhang, W. Zeng, D. Shi, S. Liu, X. Ding, B. Yang, J. Liu, K. Lam, B. Huang, X. Tao, Flexible thermoelectric generator with high Seebeck coefficients made from polymer composites and heat-sink fabrics, Commun. Mater. 3 (2022) 1–13, https://doi.org/10.1038/s43246-022-00263-1.
[11] M. Shakeel, K. Rehman, S. Ahmad, M. Amin, N. Iqbal, A. Khan, A low-cost printed organic thermoelectric generator for low-temperature energy harvesting, Renew. Energy 167 (2021) 853–860, https://doi.org/10.1016/j.renene.2020.11.158.
[12] M.R.A. Bhuiyan, H. Mamur, Ö.F. Dilmaç, M.A. Üstüner, Opportunities for thermoelectric generators in supporting a low carbon economy, Nanomater, Energy 11 (2022) 8–26, https://doi.org/10.1680/jnaen.22.00033.
[13] M.A. Zoui, S. Bentouba, J.G. Stocholm, M. Bourouis, A review on thermoelectric generators: progress and applications, Energies 13 (2020) 3606, https://doi.org/10.3390/en13143606.
[14] S. LeBlanc, Thermoelectric generators: Linking material properties and systems engineering for waste heat recovery applications, Sustain, Mater. Technol. 1–2 (2014) 26–35, https://doi.org/10.1016/j.susmat.2014.11.002.
[15] K. Yazawa, A. Shakouri, Cost-efficiency trade-off and the design of thermoelectric power generators, Environ. Sci. Technol. 45 (2011) 7548–7553, https://doi.org/10.1021/es2005418.
[16] Y.V. Kuzminskii, V.A. Zasukha, G.Y. Kuzminskaya, Thermoelectric effects in electrochemical systems. Nonconventional thermogalvanic cells, J. Power Sources 52 (1994) 231–242, https://doi.org/10.1016/0378-7753(94)02015-9.
[17] B. Yang, G. Portale, Ionic thermoelectric materials for waste heat harvesting, Colloid Polym. Sci. 299 (2021) 465–479, https://doi.org/10.1007/s00396-020-04792-4.
[18] W. Li, S. Wang, Chapter 1 - Principles of low-grade heat harvesting, in: S. Wang (Ed.), Low-Grade Therm. Energy Harvest., Woodhead Publishing, 2022: pp. 1–10. https://doi.org/10.1016/B978-0-12-823690-1.00011-3.
[19] X. Yang, P. Wang, X. Wu, Y. Liao, S. Liu, W. Duan, Y. Yue, Exploring the mechanism, advancements, and application of thermogalvanic effect in hydrogels, Preprints (2023), https://doi.org/10.22541/au.168837445.53756814/v1.
[20] W. Zhao, Z. Wang, R. Hu, X. Luo, Gel-based thermocells for low-grade heat harvesting, Europhys. Lett. 135 (2021) 26001, https://doi.org/10.1209/0295-5075/ac2075.
[21] A. Gunawan, C.-H. Lin, D.A. Buttry, V. Mujica, R.A. Taylor, R.S. Prasher, P. E. Phelan, Liquid thermoelectrics: review of recent and limited new data of thermogalvanic cell experiments, Nanoscale Microscale Thermophys. Eng. 17 (2013) 304–323, https://doi.org/10.1080/15567265.2013.776149.
[22] B. Yu, J. Duan, H. Cong, W. Xie, R. Liu, X. Zhuang, H. Wang, B. Qi, M. Xu, Z. L. Wang, J. Zhou, Thermosensitive crystallization–boosted liquid thermocells for low-grade heat harvesting, Science 370 (2020) 342–346, https://doi.org/10.1126/science.abd6749.
[23] Y. Liu, S. Zhang, Y. Zhou, M.A. Buckingham, L. Aldous, P.C. Sherrell, G.G. Wallace, G. Ryder, S. Faisal, D.L. Officer, S. Beirne, J. Chen, Advanced wearable thermocells for body heat harvesting, Adv. Energy Mater. 10 (2020) 2002539, https://doi.org/10.1002/aenm.202002539.
[24] Y. Xiang, X. Guo, H. Zhu, Q. Zhang, S. Zhu, Aqueous biphase-boosted liquid-state thermocell for continuous low-grade heat harvesting, Chem. Eng. J. 461 (2023) 142018, https://doi.org/10.1016/j.cej.2023.142018.
[25] Y. Zong, H. Li, X. Li, J. Lou, Q. Ding, Z. Liu, Y. Jiang, W. Han, Bacterial cellulose-based hydrogel thermocells for low-grade heat harvesting, Chem. Eng. J. 433 (2022) 134550, https://doi.org/10.1016/j.cej.2022.134550.
[26] Y. Chen, Q. Huang, T.-H. Liu, X. Qian, R. Yang, Effect of solvation shell structure on thermopower of liquid redox pairs, EcoMat n/a (n.d.) e12385. https://doi.org/10.1002/eom2.12385.
[27] A. Taheri, D.R. MacFarlane, C. Pozo-Gonzalo, J.M. Pringle, Application of a water-soluble cobalt redox couple in free-standing cellulose films for thermal energy harvesting, Electrochim. Acta 297 (2019) 669–675, https://doi.org/10.1016/j.electacta.2018.11.208.
[28] J. Wu, J.J. Black, L. Aldous, Thermoelectrochemistry using conventional and novel gelled electrolytes in heat-to-current thermocells, Electrochim. Acta 225 (2017) 482–492, https://doi.org/10.1016/j.electacta.2016.12.152.
[29] D. Zhang, Y. Mao, F. Ye, Q. Li, P. Bai, W. He, R. Ma, Stretchable thermogalvanic hydrogel thermocell with record-high specific output power density enabled by ion-induced crystallization, Energy Environ. Sci. 15 (2022) 2974–2982, https://doi.org/10.1039/D2EE00738J.
[30] M.A. Buckingham, S. Hammoud, H. Li, C.J. Beale, J.T. Sengel, L. Aldous, A fundamental study of the thermoelectrochemistry of ferricyanide/ferrocyanide: cation, concentration, ratio, and heterogeneous and homogeneous electrocatalysis effects in thermogalvanic cells, Sustain, Energy Fuels 4 (2020) 3388–3399, https://doi.org/10.1039/D0SE00440E.
[31] G. Qian, X. Yu, Z. Li, J. Wu, R. Huang, Y. Lu, Experimental investigation of a U-tube thermocell under various Fe(CN)63−/4− concentration, Energy Convers. Manag. 217 (2020) 113005, https://doi.org/10.1016/j.enconman.2020.113005.
[32] A. Gunawan, H. Li, C.-H. Lin, D.A. Buttry, V. Mujica, R.A. Taylor, R.S. Prasher, P. E. Phelan, The amplifying effect of natural convection on power generation of thermogalvanic cells, Int. J. Heat Mass Transf. 78 (2014) 423–434, https://doi.org/10.1016/j.ijheatmasstransfer.2014.07.007.
[33] D. Inoue, Y. Fukuzumi, Y. Moritomo, Volume effect of organic solvent on electrochemical Seebeck coefficient of [Fe(CN)6]4−/[Fe(CN)6]3− in water, Jpn. J. Appl. Phys. 59 (2020) 037001, https://doi.org/10.35848/1347-4065/ab731d.
[34] J. Li, Z. Wang, S.A. Khan, N. Li, Z. Huang, H. Zhang, Self-powered information conversion based on thermogalvanic hydrogel with interpenetrating networks for nursing aphasic patients, Nano Energy 113 (2023) 108612, https://doi.org/10.1016/j.nanoen.2023.108612.
[35] C.-G. Han, X. Qian, Q. Li, B. Deng, Y. Zhu, Z. Han, W. Zhang, W. Wang, S.-P. Feng, G. Chen, W. Liu, Giant thermopower of ionic gelatin near room temperature, Science 368 (2020) 1091–1098, https://doi.org/10.1126/science.aaz5045.
[36] Y. Wang, Y. Zhang, X. Xin, J. Yang, M. Wang, R. Wang, P. Guo, W. Huang, A. J. Sobrido, B. Wei, X. Li, In situ photocatalytically enhanced thermogalvanic cells for electricity and hydrogen production, Science 381 (2023) 291–296, https://doi.org/10.1126/science.adg0164.
[37] B. Yu, W. Yang, J. Li, W. Xie, H. Jin, R. Liu, H. Wang, X. Zhuang, B. Qi, S. Liu, L. Huang, B. Hu, J. Duan, J. Zhou, Heat-triggered high-performance thermocells enable a self-powered forest fire alarm, J. Mater. Chem. A 9 (2021) 26119–26126, https://doi.org/10.1039/D1TA06793A.
[38] J. Duan, B. Yu, L. Huang, B. Hu, M. Xu, G. Feng, J. Zhou, Liquid-state thermocells: Opportunities and challenges for low-grade heat harvesting, Joule 5 (2021) 768–779, https://doi.org/10.1016/j.joule.2021.02.009.
[39] Y. Tian, X. Yang, K. Li, Q. Zhang, Y. Li, H. Wang, C. Hou, High-performance ionic thermoelectric materials and emerging applications of ionic thermoelectric devices, Mater. Today Energy 36 (2023) 101342, https://doi.org/10.1016/j.mtener.2023.101342.
[40] J. Duan, G. Feng, B. Yu, J. Li, M. Chen, P. Yang, J. Feng, K. Liu, J. Zhou, Aqueous thermogalvanic cells with a high Seebeck coefficient for low-grade heat harvest, Nat. Commun. 9 (2018) 5146, https://doi.org/10.1038/s41467-018-07625-9.
[41] T. Kim, J.S. Lee, G. Lee, H. Yoon, J. Yoon, T.J. Kang, Y.H. Kim, High thermopower of ferri/ferrocyanide redox couple in organic-water solutions, Nano Energy 31 (2017) 160–167, https://doi.org/10.1016/j.nanoen.2016.11.014.
[42] Y. Liu, Q. Zhang, G.O. Odunmbaku, Y. He, Y. Zheng, S. Chen, Y. Zhou, J. Li, M. Li, K. Sun, Solvent effect on the Seebeck coefficient of Fe2+/Fe3+ hydrogel thermogalvanic cells, J. Mater. Chem. A (2022), https://doi.org/10.1039/D1TA10508F.
[43] X. Chen, Q. Zhang, Atomic insights into the fundamental interactions in lithium battery electrolytes, Acc. Chem. Res. 53 (2020) 1992–2002, https://doi.org/10.1021/acs.accounts.0c00412.
[44] N.N. Rajput, V. Murugesan, Y. Shin, K.S. Han, K.C. Lau, J. Chen, J. Liu, L.A. Curtiss, K.T. Mueller, K.A. Persson, Elucidating the solvation structure and dynamics of lithium polysulfides resulting from competitive salt and solvent interactions, Chem. Mater. 29 (2017) 3375–3379, https://doi.org/10.1021/acs.chemmater.7b00068.
[45] B. Yu, H. Xiao, Y. Zeng, S. Liu, D. Wu, P. Liu, J. Guo, W. Xie, J. Duan, J. Zhou, Cost-effective n-type thermocells enabled by thermosensitive crystallizations and 3D multi-structured electrodes, Nano Energy 93 (2022) 106795, https://doi.org/10.1016/j.nanoen.2021.106795.
[46] T. Kim, W. Choi, H.-C. Shin, J.-Y. Choi, J.M. Kim, M.-S. Park, W.-S. Yoon, Applications of voltammetry in lithium ion battery research, J. Electrochem. Sci. Technol. 11 (2020) 14–25, https://doi.org/10.33961/jecst.2019.00619.
[47] J. Heinze, M. Dietrich, Cyclic voltammetry as a tool for characterizing conducting polymers, Mater. Sci. Forum 42 (1989) 63–78, https://doi.org/10.4028/www.scientific.net/MSF.42.63.
[48] P.T. Kissinger, W.R. Heineman, Cyclic voltammetry, J. Chem. Educ. 60 (1983) 702, https://doi.org/10.1021/ed060p702.
[49] W. Liu, H.S. Kim, Q. Jie, Z. Ren, Importance of high power factor in thermoelectric materials for power generation application: A perspective, Scr. Mater. 111 (2016) 3–9, https://doi.org/10.1016/j.scriptamat.2015.07.045.
[50] X. Yu, Z. Shen, G. Qian, G. Lu, H. Liu, R. Huang, Z. Li, Synergistic improvement of Seebeck coefficient and power density of an aqueous thermocell using natural convection for low-grade heat utilization, Appl. Therm. Eng. 231 (2023) 121004, https://doi.org/10.1016/j.applthermaleng.2023.121004.
[51] Y. Tanaka, A. Wake, D. Inoue, Y. Moritomo, Concentration gradient effect in liquid thermoelectric device composed of organic-solvent-added aqueous solution containing K4[Fe(CN)6]/K3[Fe(CN)6], Jpn. J. Appl. Phys. 63 (2024) 014002, https://doi.org/10.35848/1347-4065/ad1424.
[52] L. Zhang, T. Kim, N. Li, T.J. Kang, J. Chen, J.M. Pringle, M. Zhang, A.H. Kazim, S. Fang, C. Haines, D. Al-Masri, B.A. Cola, J.M. Razal, J. Di, S. Beirne, D. R. MacFarlane, A. Gonzalez-Martin, S. Mathew, Y.H. Kim, G. Wallace, R. H. Baughman, High power density electrochemical thermocells for inexpensively harvesting low-grade thermal energy, Adv. Mater. 29 (2017) 1605652, https://doi.org/10.1002/adma.201605652.

[53] H. Im, T. Kim, H. Song, J. Choi, J.S. Park, R. Ovalle-Robles, H.D. Yang, K.D. Kihm, R.H. Baughman, H.H. Lee, T.J. Kang, Y.H. Kim, High-efficiency electrochemical thermal energy harvester using carbon nanotube aerogel sheet electrodes, Nat. Commun. 7 (2016) 10600, https://doi.org/10.1038/ncomms10600.
[54] R. Hu, B.A. Cola, N. Haram, J.N. Barisci, S. Lee, S. Stoughton, G. Wallace, C. Too, M. Thomas, A. Gestos, M.E. dela Cruz, J.P. Ferraris, A.A. Zakhidov, R. H. Baughman, Harvesting waste thermal energy using a carbon-nanotube-based thermo-electrochemical cell, Nano Lett. 10 (2010) 838–846, https://doi.org/10.1021/nl903267n.
[55] G. Li, D. Dong, G. Hong, L. Yan, X. Zhang, W. Song, High-efficiency cryo-thermocells assembled with anisotropic holey graphene aerogel electrodes and a eutectic redox electrolyte, Adv. Mater. 31 (2019) 1901403, https://doi.org/10.1002/adma.201901403.
[56] Y. Liu, H. Wang, P.C. Sherrell, L. Liu, Y. Wang, J. Chen, Potentially wearable thermo-electrochemical cells for body heat harvesting: from mechanism, materials, strategies to applications, Adv. Sci. 8 (2021) 2100669, https://doi.org/10.1002/advs.202100669.
[57] E. Garofalo, M. Bevione, L. Cecchini, F. Mattiussi, A. Chiolerio, Waste heat to power: technologies, Current Applications, and Future Potential, Energy Technol. 8 (2020) 2000413, https://doi.org/10.1002/ente.202000413.
[58] Y. Jia, Q. Jiang, H. Sun, P. Liu, D. Hu, Y. Pei, W. Liu, X. Crispin, S. Fabiano, Y. Ma, Y. Cao, Wearable thermoelectric materials and devices for self-powered electronic systems, Adv. Mater. 33 (2021) 2102990, https://doi.org/10.1002/adma.202102990.
[59] Y. Chen, Q. Huang, T.-H. Liu, X. Qian, R. Yang, Effect of solvation shell structure on thermopower of liquid redox pairs, EcoMat 5 (2023) e12385.
[60] P.F. Salazar, S. Kumar, B.A. Cola, Design and optimization of thermo-electrochemical cells, J. Appl. Electrochem. 44 (2014) 325–336, https://doi.org/10.1007/s10800-013-0638-y.